Nanoscale Advances

ROYAL SOCIETY OF CHEMISTRY

PAPER

View Article Online
View Journal | View Issue

Cite this: *Nanoscale Adv.*, 2025, **7**, 3764

Synthesis of $CsPbBr_3$ decorated ZIF-8 nanocomposite for enhanced photocatalytic performance†

Alen Sam Thomas, [a] Philip Nathaniel Immanuel,[a] Neena Prasad, [a] Achiad Goldreich,[a] Jonathan Prilusky,[a] Raanan Carmieli[b] and Lena Yadgarov *[a]

$CsPbBr_3$ (CPB) perovskite nanocrystals (NCs) have attracted considerable interest due to their outstanding charge carrier mobility, long diffusion lengths, and efficient visible light absorption, making them ideal candidates for photocatalysis, light-emitting diodes (LEDs), solar cells, and photodetectors. However, their practical applications are limited by poor environmental stability. To address this challenge, we employ a zeolitic imidazolate framework (ZIF), specifically ZIF-8, as a stabilizing matrix for its exceptional thermal and chemical stability, high surface area, and versatile synthesis routes. The CPB/ZIF-8 nanocomposite was synthesized by integrating hot-injection-produced CPB NCs with ZIF-8 using an optimized mixing approach, ensuring a uniform NCs distribution. Electron microscopy (EM) analysis confirmed the well-controlled and uniform distribution of the NCs on the surface of the ZIF-8. Moreover, the Fourier-transform infrared spectroscopy (FTIR) revealed ligand exchange, where the imidazole linkers of the ZIF-8 structure replace the NCs ligands. The process advances almost epitaxial attachment of the latter, thus promoting effective charge interactions in the integration process. Indeed, we observe that upon formation of the composite, there is a 92% quenching in the photoluminescence (PL) of the NCs. This finding further indicates efficient charge separation and reduced electron–hole recombination. To gain deeper insight into the charge transfer mechanisms, we conducted electron paramagnetic resonance (EPR) measurements to compare the radical generation capabilities of CPB and ZIF with those of the CPB/ZIF composite. The composite exhibited superior radical generation capabilities, particularly hydroxyl radicals (•OH), indicating enhanced charge transfer. These findings suggest that the composite is a highly promising candidate for photocatalysis. Building on these findings, we explored the photocatalytic abilities of the composite through dye degradation experiments, using methyl orange (MO) and bromocresol green (BCG) as model dyes. The CPB/ZIF nanocomposite demonstrated significantly enhanced photocatalytic performance compared to pristine ZIF and CPB NCs. Specifically, its degradation rates were 1.48× and 1.75× higher for MO and BCG, respectively, than those of CPB NCs. This improvement highlights the effective interaction between CPB NCs and ZIF, establishing the CPB/ZIF nanocomposite as a promising material for photocatalysis and optoelectronic applications.

Received 4th March 2025
Accepted 18th April 2025

DOI: 10.1039/d5na00217f

rsc.li/nanoscale-advances

Introduction

Metal-halide perovskites (MHPs) have emerged as highly promising materials due to their exceptional properties and versatile applications in photovoltaics, optoelectronics, and photocatalysis.[1,2] These compounds possess exceptional optical and electronic properties, including a high absorption coefficient, a direct and tunable bandgap, long carrier diffusion lengths, high charge mobility, and low recombination losses.[3] The general crystal structure of MHPs is ABX_3, where A is typically an organic or inorganic cation (Methylammonium, Cs or Rb), B is a metal cation (Pb or Sn), and X is a halide anion (Br, I, or Cl).[3] The structure consists of BX_6 octahedra, with the B cation at the center and the A cation occupying a 12-fold coordinated site. Depending on composition and conditions, perovskites can crystallize in cubic, orthorhombic, or tetragonal systems.[4] Among other MHPs, cesium lead bromide ($CsPbBr_3$) has drawn considerable interest due to its superior thermal and structural stability compared to its organic and inorganic counterparts.[5,6] $CsPbBr_3$ (CPB) can exist as bulk crystals or nanocrystals (NCs), each exhibiting distinct properties suited

[a]*Department of Chemical Engineering, Ariel University, 4070000, Israel. E-mail: lenay@ariel.ac.il*

[b]*Department of Molecular Chemistry and Materials Science, Weizmann Institute of Science, Rehovot, 7610001, Israel*

† Electronic supplementary information (ESI) available. See DOI: https://doi.org/10.1039/d5na00217f

for different applications.[7] Single crystals of CPB offer excellent charge transport properties, low defect densities, and high carrier mobility, making them ideal for optoelectronic devices such as photodetectors and solar cells.[8] However, their large size limits their processability and surface area, which is critical for applications like photocatalysis and light emission.[9,10] In contrast, CPB NCs exhibit outstanding optoelectronic properties, such as high photoluminescence quantum yield, high charge carrier mobility, and high absorption coefficient in the visible light range.[5,11] These materials are widely used in photocatalytic CO_2 reduction, fluorescence sensing, and optoelectronic devices.[12–14] To achieve superior optical properties, selecting an optimal synthesis method for CPB is essential. Previous reports have shown that the hot injection (HI) method outperforms other approaches in terms of quality and optical performance.[15]

Despite these promising features, one of the most critical challenges for CPB NCs remains their stability.[16] The ionic crystal structure makes them less resistant to chemical and physical vulnerabilities such as heat, polar solvents, light, and oxygen.[17] CPB NCs are highly sensitive to polar solvents and harsh reaction environments, which can lead to rapid decomposition.[5] Researchers have explored various strategies, including surface passivation, encapsulation, and interface engineering, to address the instability of perovskite-based devices and extend their operational lifespan.[18,19] In this context, metal–organic frameworks (MOFs) have emerged as a promising approach to significantly enhancing CPB stability by encapsulation.[20] Structurally, MOFs consist of single or mixed metal ions coordinated with organic linkers (ligands) to form a porous framework, enabling applications in gas storage, supercapacitors, and photocatalytic dye degradation. The MOF materials pose high crystallinity, large surface area, excellent porosity, and remarkable environmental stability.[21,22] Thus, these materials can effectively shield CPB from external environmental factors by providing a protective barrier, thereby reducing degradation and improving long-term performance. Furthermore, MOFs are among the most effective catalysts due to their large surface area and strong light-harvesting ability. These properties significantly enhance the performance of CPB-MOF-based nanocomposites, particularly in photocatalytic applications.[23,24]

Notably, most studies focus on encapsulating CPB NCs with MOFs to enhance their stability and performance.[25,26] While encapsulation has shown promise in enhancing CPB's environmental stability, it faces challenges such as incomplete pore filling, partial encapsulation, and limited control over nanocrystal size.[27] Additionally, synthesizing MOF-encapsulated CPB is typically complex and involves multiple steps.[26,28] Furthermore, complete encapsulation can hinder efficient charge transfer between CPB and its surroundings, potentially compromising performance, including low quantum yield, and compromising the activity of this material as a photocatalyst.[29]

Decorating CPB NCs onto MOFs presents a highly effective approach for photocatalytic applications, offering several key advantages. This method preserves the high quantum yield of CPB NCs without compromising their optical properties while simultaneously enhancing the optical activity of both components.[30] The exposed NCs on the MOF surface facilitate superior light absorption, significantly boosting photocatalytic performance.[31] Additionally, this structured decoration enhances charge transfer between CPB NCs and MOFs, thus promoting charge separation, a crucial factor for efficient photocatalysis.[32] Indeed, studies on similar composite systems, such as CPB-MIL-100, have demonstrated improved charge transfer.[33] The ability to precisely control NCs' size allows for fine-tuning absorption bands, optimizing the material for specific light wavelengths.[34] Beyond photocatalysis, this approach holds great potential for applications such as sensing, where the high quantum yield and improved charge transfer efficiency of CPB NCs can be fully leveraged without the constraints of complete encapsulation.[35]

Among the different MOFs, zeolitic imidazolate framework-8 (ZIF-8) is particularly well-suited for forming composites with CPB NCs. It can be synthesized under mild conditions, such as room temperature, and exhibits exceptional properties like high porosity and a large surface area.[36] Moreover, ZIF-8 is compatible with non-polar solvents, making it well-suited for integrating with CPB without compromising its stability.[23] The versatile synthesis routes enable precise tailoring to specific requirements, facilitating the integration of NCs with ZIF-8 to create a stable composite.[22,23] Previous studies on synthesizing CPB/ZIF-8 nanocomposites have predominantly focused on encapsulation methods.[35,37] In the encapsulation method, the NCs nucleate and grow within the pores of ZIF-8, following a confined growth mechanism.[38] Research on related systems highlights how ZIF-8's high surface area and porous nanostructure provide abundant active sites for adsorption and catalysis.[39] However, the development of uniformly decorated CPB/ZIF-8 composites remains a promising research direction with the potential to enhance photocatalytic performance significantly. This approach is expected to improve light harvesting, charge separation, and catalytic activity, making it a compelling alternative to traditional encapsulation techniques.

Uniformly decorating CPB NCs onto ZIF-8 offers significant advantages. This decoration process enhances the overall performance of the nanocomposite by improving charge transfer efficiency and increasing the available surface area for photocatalytic reactions.[40,41] This reduces recombination and increases the overall photocatalytic performance. However, achieving a stable and well-distributed nanocomposite remains challenging. Although the encapsulation method is well studied and understood, the precise mechanism behind the uniform distribution of NCs on ZIF-8 remains unclear. A comprehensive understanding of these processes is crucial for optimizing material performance and advancing CPB/ZIF-8-based photocatalytic applications.[42] While ligand exchange is a potential pathway, other processes may also play a role in the decoration process.[43] Gaining insight into this mechanism is crucial for ensuring uniform decoration. Precise control over ligand exchange and surface interactions is necessary to facilitate proper integration, minimize defects, and enhance charge transfer efficiency.[44] Additionally, the charge transfer dynamics

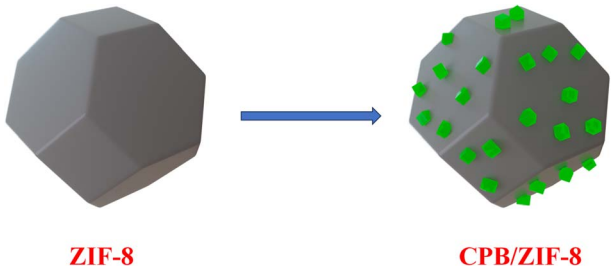

Scheme 1 Schematic representation of ZIF-8 to CPB/ZIF-8 nanocomposite.

between CPB NCs and ZIF-8 remain largely unexplored, yet they play a crucial role in determining photocatalytic efficiency.[45] Studying how CPB NCs interact with ZIF-8 to enhance light absorption, charge separation, and reaction kinetics will be crucial in proving the underlying photocatalytic mechanism.

Here, we present a straightforward and effective synthesis method for preparing uniformly distributed NCs in the CPB/ZIF-8 nanocomposite (Scheme 1). Our research focuses on elucidating three critical aspects: the decoration mechanism, the nature of charge transfer, and understanding the photocatalytic mechanism. We employed Fourier-transform infrared (FTIR) spectroscopy to confirm that ligand exchange is the primary driving force behind composite formation. The analysis showed that the ligands of CPB NCs were partially replaced by the imidazole ligands of ZIF-8. This provided valuable insights into the chemical interactions within the composite. Electron microscopy (EM) analysis revealed a uniform distribution of CPB NCs over ZIF-8, driven by ligand exchange, offering a further understanding of the possible surface interactions. The unshifted absorbance spectra of CPB NCs in the composite indicated the preservation of their structural integrity. To investigate charge transfer within the composite, we conducted photoluminescence (PL) studies. The results revealed an impressive 92% PL quenching, indicating highly efficient charge transfer between CPB NCs and ZIF-8. Electron paramagnetic resonance (EPR) analysis provided insights into charge dynamics, demonstrating enhanced radical generation by the composite, particularly hydroxyl radicals (˙OH). These results highlight its strong potential for photocatalysis. The photocatalytic performance of the composite was evaluated using dye degradation as a model reaction, both to assess its real-world applicability and to understand the charge transfer process further. The CPB/ZIF-8 composite exhibited significantly enhanced dye degradation efficiency compared to its pristine components, validating its improved photocatalytic activity. This study unveiled the mechanism of uniform decoration, elucidated the efficient charge transfer process, and confirmed the photocatalytic mechanism, providing a comprehensive understanding of the CPB/ZIF-8 nanocomposite's enhanced performance.

Experimental section

Synthesis of ZIF-8

ZIF-8 was synthesized based on the previous reports.[22] Specifically, 297 mg (1 mM) of zinc nitrate (Zn $(NO_3)_2 \cdot 6H_2O$) and 656 mg (8 mM) of 2-methylimidazole were dissolved separately in 12 mL of methanol. The 2-methylimidazole solution was slowly added to the zinc nitrate solution and stirred for 6 h at room temperature (RT). The resulting white precipitate was collected by centrifugation (6000 rpm, 10 min) and washed with methanol (3 × 30 mL) to remove excess ligands. The white residue was dried overnight in a vacuum oven at 70 °C to obtain ZIF-8.

Synthesis of $CsPbBr_3$ NCs (CPB NCs)

The hot-injection method was employed for the synthesis of high-quality CPB NCs, enabling precise control over their size, morphology, and optical properties.[46] This process consists of three critical steps: the synthesis of the cesium oleate precursor, the preparation of the lead precursor solution, and the final hot-injection step, which induces rapid nucleation and growth of the nanocrystals.

Preparation of Cs-oleate solution: cesium oleate solution was prepared by dissolving 40.8 mg (0.125 mM) of cesium carbonate (Cs_2CO_3) and 126 μL (0.361 mM) of oleic acid (OA) in 2 mL of octadecane (ODE) at 120 °C. The mixture was vacuumed for an hour with continuous stirring. Afterward, the mixture was placed under a nitrogen (N_2) flow, and the temperature was raised to 150 °C for an additional hour, at which point the solution became transparent, indicating readiness for the next synthetic step.

Preparation of lead precursor solution: in parallel, a three-neck flask was loaded with 69 mg (0.188 mmol) of lead bromide ($PbBr_2$) and 5 mL of ODE, such that the final concentration of the $PbBr_2$ was 37.6 mM. The mixture was stirred under a vacuum at 120 °C for 1 hour to remove impurities and residual moisture. Simultaneously, another vial containing 1 mL of OA and 1 mL of oleylamine (OLA) was heated at 120 °C under vacuum with continuous stirring for 1 h. After this, 1 mL of the OA/OLA mixture was injected into the $PbBr_2$ solution, and the temperature was increased to 170 °C under an N_2 atmosphere to dissolve $PbBr_2$ completely.

Hot-injection: once $PbBr_2$ was fully dissolved, the N_2 atmosphere was temporarily removed, and 0.4 mL of the previously prepared cesium oleate solution was swiftly injected into the lead precursor solution at 170 °C. Within 5 seconds, the reaction was quenched by immersing the flask in an ice-water bath to reduce the temperature below 10 °C rapidly. The cooled solution was then equilibrated to RT. The reaction mixture was centrifuged at 11 000 rpm for 10 minutes, and the resulting precipitate containing $CsPbBr_3$ NCs was collected. The obtained NCs were redispersed in 6 mL hexane and stored for further characterization.

Synthesis of $CsPbBr_3$/ZIF-8 (CPB/ZIF-8)

The $CsPbBr_3$/ZIF-8 (CPB/ZIF-8) nanocomposite was synthesized using two approaches: a one-pot synthesis method (detailed in the ESI, Section 1, Fig. S1†) and a simple mixing process involving pre-prepared CPB nanocrystals and ZIF-8 nanoparticles (described below). SEM analysis revealed that the one-pot synthesis led to aggregated structures, where CPB covered

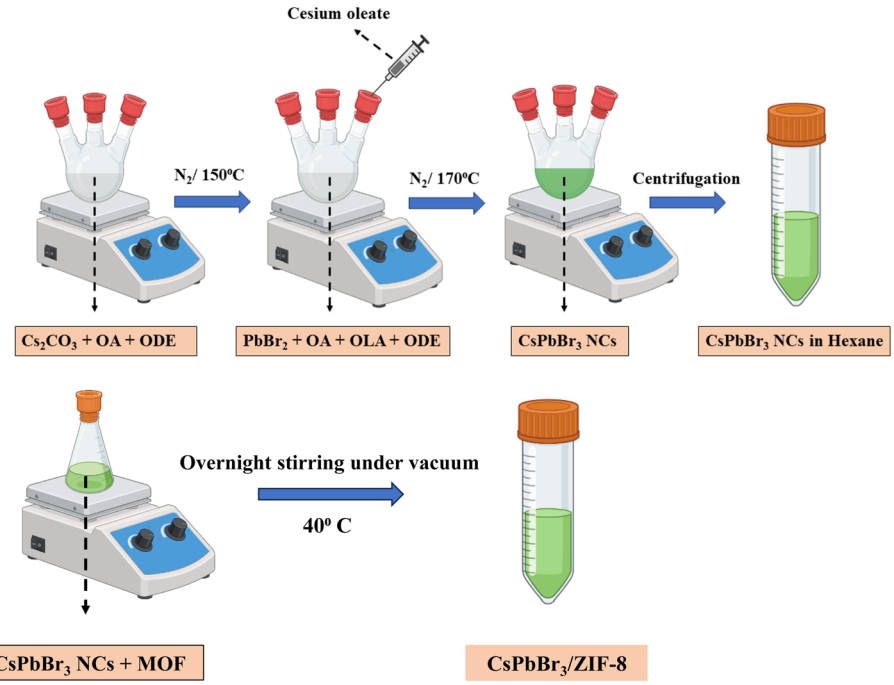

Scheme 2 Schematic representation of the synthesis CPB/ZIF-8.

and disrupted the ZIF-8 framework, contrary to the intended encapsulation design. The 'one-pot' synthesized composite exhibited inferior morphological, structural, and optical properties compared to the CPB-decorated ZIF-8. Consequently, we discontinued further experiments and characterization of this material.

The composites comprising ZIF-8 decorated with CPB nanocrystals were prepared through a straightforward mixing process. Initially, 30 mg of ZIF-8 powder was dispersed in 2 mL of hexane and sonicated for 5 minutes to achieve uniform dispersion. Subsequently, 3 mL of $CsPbBr_3$ (CPB) solution in hexane was introduced into the ZIF-8 dispersion. The mixture was again sonicated for 5 minutes to ensure uniform mixing, followed by stirring under a vacuum at 50 °C overnight to facilitate the efficient incorporation of CPB NCs into the ZIF-8 framework. The precipitate formed was collected by centrifugation at 9000 rpm for 10 minutes and washed with hexane (2 × 10 mL) to remove the excess NCs. Finally, the purified CPB/ZIF-8 nanocomposite was dried under vacuum at 50 °C for 6 h. This method yielded a highly uniform CPB/ZIF-8 nanocomposite, ensuring effective interaction between the CPB NCs and the ZIF-8 framework. The synthesis procedure is illustrated schematically in Scheme 2.

Characterization methods

The X-ray diffraction (XRD) pattern was recorded in the 2θ range 5–50° using a Rigaku SmartLab diffractometer with a Cu anode (Cu Kα radiation with 1.5418 Å wavelength) operated at 40 kV and 120 mA. The morphology of the samples was observed *via* scanning electron microscopy (SEM) using a Tescan MAIA3 instrument equipped with an energy dispersive spectrometer (EDS) detector and Thermo Fisher Scientific™ Talos™ F200X transmission electron microscope (TEM). The FTIR-6800, Jasco, Japan, was used to perform Fourier transform infrared spectrometer (FTIR) measurements in the spectral region of 3500 to 400 cm^{-1}.

Electron paramagnetic resonance (EPR) spectra were recorded on a Bruker ELEXSYS 500 X-band spectrometer equipped with a Bruker ER4102ST resonator in a Wilmad flat cell for aqueous solutions (WG-808-Q) at RT. Experimental conditions were 512 points, with a microwave power of 20 mW, 0.1 mT modulation amplitude, and 100 kHz modulation frequency. The sweep range was 200 mT.

The UV-vis absorption was measured in the range of 300 to 800 nm, and photoluminescence (PL) spectra were recorded with an excitation wavelength of 320 nm in the range of 360 to 700 nm using the Jasco V-750 spectrophotometer and Jasco FP-8350 fluorometer, respectively.

Photocatalysis

Photocatalytic dye degradation experiments were conducted using a solar simulator (Xenon lamp) with a power output and light intensity of 485 mW cm^{-2}, equipped with a UV cut-off filter. A solvent mixture of 25 mL consisting of 10% (v/v) ethanol in toluene was used for all experiments. Methyl orange (MO) and bromocresol green (BCG) are selected as the model dyes for the degradation studies. The amount and the concentration of the catalyst and dye were maintained at 10 mg and 16 ppm, respectively, across all trials to ensure consistency. Prior to degradation, the catalyst and dye were dispersed *via* sonication for 5 minutes to ensure homogeneity. All measurements were performed at ambient temperature under

continuous stirring to maintain uniform reaction conditions. Among the dyes used, BCG is a pH indicator that changes color depending on the pH of the solution. It transitions from yellow at low pH to blue at high pH, with a transition range between pH 3.8 and 5.4. To address the high pH dependency, we stirred the BCG solution in the dark for 30 minutes following the addition of the catalyst to allow pH stabilization.[47]

EPR measurements

The EPR measurements are carried out at room temperature using a Bruker ELEXYS E500 spectrometer operating at X-band frequencies (9.5 GHz) and a Bruker ER4119HS resonator. The spin trap solution (25 mM) was prepared by first dissolving 50 mg of BMPO (MW 199.25, Dojindo Molecular Technologies, Inc.) in 10 mL of absolute EtOH (99.5%, Baker HPLC Analyzed, J.T. Baker). For the sample solution, 1 mg sample powder was first dispersed in 3 mL of toluene by sonication for 5 min. For the measurements, 180 μL of sample solution was mixed with 20 μL of the spin trap solution (10% v/v EtOH in Toluene) using a vortex. Samples were loaded into Vitrocom quartz capillaries, CV1012-Q-100, with a 1 mm inner diameter. The experimental conditions of the EPR spectral analysis were as follows: microwave power of 20 mW, 0.1 mT modulation amplitude, and 100 kHz modulation frequency. The sweep range was 10 mT, and the spectra consisted of 512 points. The samples were irradiated under white light using a SCHOTT KL 2500 LED light source with a maximum intensity of 1100 lm. EPR spectra were recorded every 6 minutes under both illumination and dark conditions. In order to assess the radical quenching effects, 10 μL of DMSO was added as a hydroxyl radical quencher to the designated samples, and EPR spectra were subsequently recorded under illumination for 6 minutes.

Results and discussion

Morphological analysis

SEM and TEM. SEM and TEM analyses investigated the morphology and formation of ZIF-8, CPB NCs, and the CPB/ZIF-8 nanocomposite (Fig. 1). The SEM/TEM micrographs in Fig. 1a and b highlight the truncated rhombic dodecahedral and cubic morphology typical of ZIF-8 and CPB, respectively.[22] The average size of ZIF-8 is 66.553 ± 8.01 nm, while for the CPB NCs, it is 15.55 ± 2.6. The size distribution calculations are provided in the ESI.† Fig. S2 and S3† demonstrate a relatively uniform size distribution for both CPB NCs and ZIF. The EDS analysis of the CPB/ZIF-8 nanocomposite, presented in Fig. 1c, reveals characteristic elemental signatures from both ZIF-8 and CPB, providing conclusive evidence of their successful incorporation into composite structure. Further TEM analysis (Fig. 1d and e) confirms this result, showing dark dot-like structures identified as CPB NCs decorating the ZIF-8 surface. The lattice spacing of CPB NCs (Fig. 1f), measured at 0.42 nm, corresponds to the (110) planes of the orthorhombic phase of the CPB crystal structure, providing additional confirmation of the nanocomposite formation.[48,49]

Notably, this uniform distribution of NCs on the surface of ZIF was not a straightforward outcome. The primary challenge

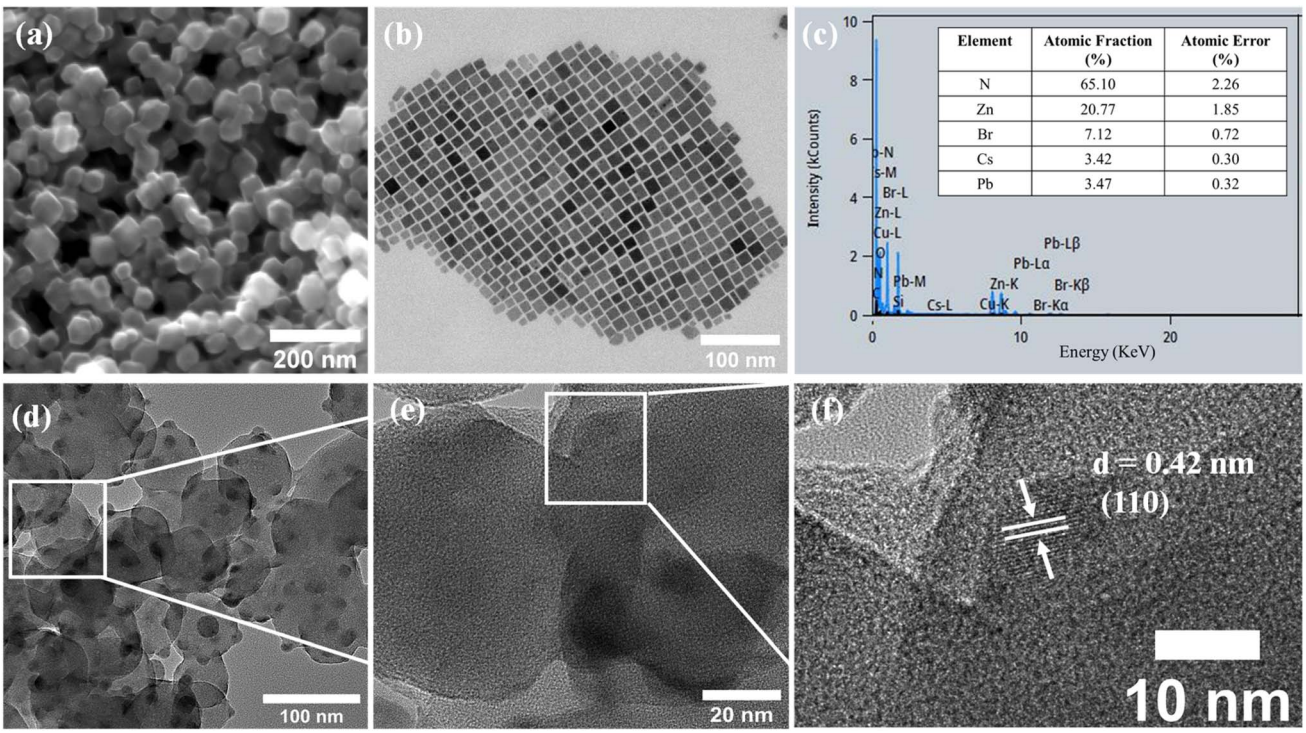

Fig. 1 (a) SEM micrograph of ZIF-8, (b) TEM micrograph of CPB NC, (c) EDS spectra of CPB/ZIF-8 nanocomposite, and (d) TEM micrograph of the CPB/ZIF-8 nanocomposite (e) magnified TEM micrograph CPB/ZIF-8 nanocomposite and (f) Lattice fringes of the CPB NC in the nanocomposite.

lies in the instability of CPB NCs in polar solvents, coupled with the poor dispersibility of ZIF-8 in non-polar solvents. Thus, it is crucial to identify suitable conditions to accommodate both constraints. We chose hexane for its low polarity, which maintains the stability of the CPB nanocrystals. To enhance the distribution of ZIF-8, we ultrasonicated it in hexane for 30 minutes, pausing every 10 minutes. We then combined the two solutions, ultrasonicated them for an additional 10 minutes, and stirred the mixture under a vacuum at 50 °C for 12 h.

Another challenge in achieving uniform dispersion of CPB NCs within the ZIF-8 framework is their strong tendency to aggregate, which can compromise structural homogeneity and alter optical properties.[50,51] The prolonged stirring and slight temperature increase improved the distribution of CPB NCs over the ZIF-8 surface in several ways. First, prolonged stirring and mixing ensures better dispersion of precursors, enhancing the interaction between the components and increasing the stability of the nanocomposite.[20] Secondly, the elevated temperature raises the kinetic energy of the NCs, causing them to move more rapidly and vigorously.[52] The higher molecular speed results in more frequent collisions between reactant particles, enhancing the likelihood of successful interactions.[53] Overall, prolonged stirring and a slight temperature increase synergistically promote a more uniform and stable distribution of CPB NCs over the ZIF-8 surface, enhancing the nanocomposite's quality.

To better understand the nanocomposite formation, we analyzed the sizes of the CPB NCs on the ZIF-8 and in the supernatant after mixing. The supernatant was collected *via* centrifugation following the final stage of nanocomposite formation. TEM analysis showed that the average size of CPB NCs attached to ZIF-8 was 15.54 ± 3.5 nm (Fig. S4†). The size distribution graphs exhibit symmetry with peaks centered around the mean, indicating the uniformity in the sizes of the CPB NCs on the ZIF-8. Notably, the average CPB NC size in the nanocomposite remained consistent with that of the pristine solution, which measured 15.55 ± 2.6 nm.

The average size of CPB NCs in the supernatant (Fig. S5†) decreased to 12.46 ± 5.7 nm, indicating that larger CPB particles preferentially adhered to the ZIF-8 surface during nanocomposite synthesis. This phenomenon can be attributed to the tendency of larger CPB NCs to detach from their ligands and adhere to template surfaces such as MOFs. The primary factor driving this "ligand-exchange" behavior is surface energy; larger NCs possess a greater surface area, resulting in higher surface energy, which they reduce by detaching from ligands and attaching to more stable surfaces.[54,55] Additionally, as NCs grow, their surface-to-volume ratio decreases, resulting in fewer ligand binding sites relative to their size and weaker overall ligand attachment.[54] Electrostatic interactions also play a role, as larger CPB NCs typically have a more negative surface charge, creating an initial attraction to the positively charged surfaces or metal ions in ZIF.[56,57] This is followed by ligand exchange between the ligand molecules in ZIF and the positively charged components of the CPB NCs, resulting in chemical interaction.[58] These factors collectively drive the attachment of larger NCs to MOFs with almost uniform sizes.

The area of CPB coverage over ZIF-8 was quantified using TEM imaging (Fig. S6 and Table S1†) and ImageJ software. The results indicate that approximately 24% of ZIF-8 was covered by CPB NCs. The micrographs revealed a well-spaced distribution of CPB NCs with uniform sizes, a characteristic not reported in previous studies, which typically showed either full coverage or uneven distributions of CPB NCs with varying sizes.[35,45,59] TEM analysis indicated that slightly larger CPB nanocrystals adhere to the ZIF-8 framework, exhibiting a uniform size distribution. These larger crystals are stabilized by the framework due to surface energy, ligand exchange, and electrostatic interactions.

Structural analysis

XRD. XRD analysis was performed on ZIF-8, pristine CPB, and CPB/ZIF-8 to examine the formation of nanocomposites and their structural properties, as illustrated in (Fig. 2). The diffraction pattern of CPB and ZIF-8 (Fig. 2, red and blue line, respectively) exhibits well-defined peaks corresponding with the previously reported crystalline structure (JCPDS – 01-072-7929 and JCPDS – 00-062-1030, respectively).[36,60,61] Notably, due to the random orientation of CPB NCs, the typical shoulder peaks at 15.2°, 21.5°, and 30.5° are indistinguishable.[62] Interestingly, the CPB/ZIF-8 nanocomposite exhibits only the characteristic ZIF-8 and CPB characteristic peaks for ZIF-8 and CPB. Indeed, the sharp, well-defined peaks of ZIF-8 remain intact without any noticeable broadening, confirming that its crystalline structure was preserved in the nanocomposite. The XRD results confirm the successful formation of the CPB/ZIF-8 nanocomposite, with both materials retaining their characteristic crystalline structures as evidenced by the sharp ZIF-8 peaks and distinct CPB reflections.

Chemical analysis

FTIR analysis. To further investigate the formation mechanism by comparing the functional groups and chemical compositions, we employed FTIR spectroscopy to analyze pristine ZIF-8, CPB, and the CPB/ZIF-8 nanocomposite, as shown in

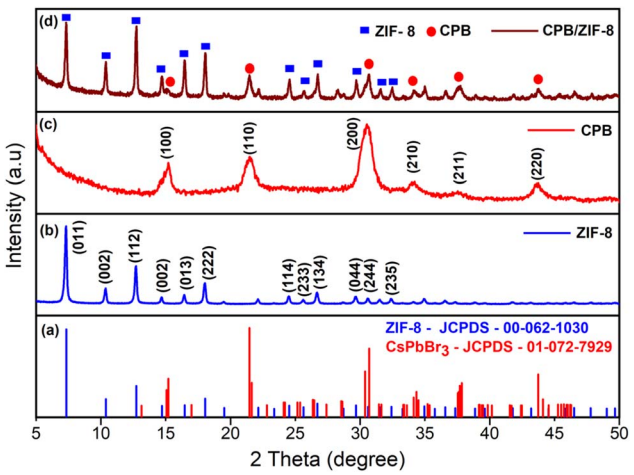

Fig. 2 XRD pattern of (a) reference spectrum, (b) ZIF-8, (c) CPB, and (d) CPB/ZIF-8 composite.

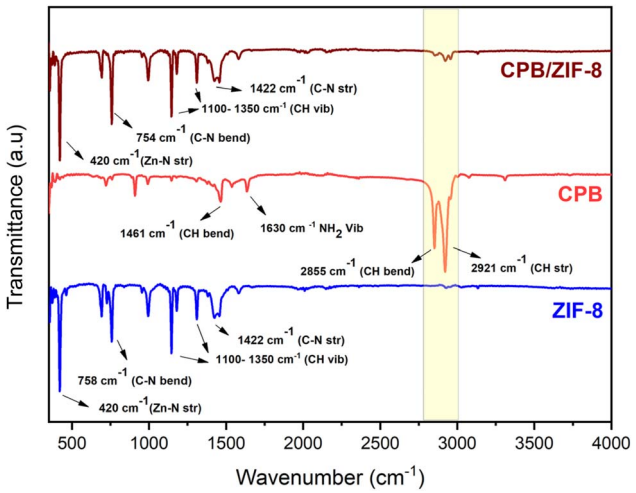

Fig. 3 FTIR spectra of ZIF-8 (bottom), CPB (middle), and CPB/ZIF-8 (top).

Fig. 3. The FTIR spectrum of pristine ZIF-8 exhibited a prominent peak at 420 cm^{-1}, corresponding to the stretching vibration of the Zn–N bond between Zn^{2+} and the 2-methylimidazole ligand.[63] Pristine CPB displayed characteristic peaks at 2848 cm^{-1} and 2917 cm^{-1}, representing its organic ligands' C–H bending and stretching vibrations.[64,65]

In the FTIR spectrum of the CPB/ZIF-8 nanocomposite, peaks corresponding to both ZIF-8 and CPB were observed. The ZIF-8 peaks exhibited significantly higher intensity than those of CPB, indicating a higher concentration of ZIF-8 per unit volume.[66] Interestingly, the CPB ligand peaks in the 2850–2950 cm^{-1} range showed a significant reduction in intensity, supporting ligand exchange alongside surface charge interactions. This reduction indicates interactions between Pb^{2+} ions from the CPB NCs and the nitrogen atoms of the imidazole ligands in ZIF-8, enabling both chemical and physical adsorption.[35,43] Such interactions promote chemical and physical adsorption, improving the adhesion of CPB nanocrystals to the ZIF-8 surface. Micrographic analysis revealed the attachment of larger CPB particles, likely driven by surface charge interactions and potential ligand exchange. FTIR results further support this observation, which provides additional confirmation of the ligand exchange process. Together, these findings reinforce the role of ligand exchange in the nanocomposite formation. Consequently, this facilitates a more uniform CPB distribution throughout the nanocomposite.

Optical analysis

UV visible spectra. The optical properties of the pristine materials and nanocomposites were analyzed using UV-vis absorption and PL spectroscopy. The absorption spectrum of ZIF-8 (Fig. S7†), measured in methanol, shows a distinct maximum at 210 nm. Due to the poor stability of CPB NCs and CPB/ZIF-8 nanocomposites in polar solvents, hexane was used as the dispersion medium for these measurements. However, as hexane is UV-active, absorption below 300 nm could not be recorded. The pristine CPB NCs and CPB/ZIF-8 exhibit absorption edges at 512 nm and 511 nm, respectively (Fig. 4a). The negligible shift in the absorption edge between pristine CPB and the nanocomposite confirms that the optical activity of the CPB NCs remains intact within the CPB/ZIF-8.

The Tauc equation was used to calculate the materials' optical band gap (E_g), and the corresponding graphs are provided in the ESI (Fig. S8).† The band gap (E_g) values of ZIF-8, CPB NCs, and CPB/ZIF-8 were determined to be 5.35 eV, 2.32 eV, and 2.32 eV, respectively (Table S2†). The optical band gap analysis indicates no significant change between the CPB NCs and the CPB/ZIF-8 composite, confirming that the CPB NCs contribute significantly to the composite's optical activity.

Photoluminescence (PL) spectra. Fig. 4b presents the PL spectra of CPB NCs and CPB/ZIF-8 composites. The CPB NCs exhibit an intense green fluorescence peak at 513 nm, while the PL emission peak of CPB/ZIF-8 is observed at 517 nm. The slight red shift observed in the PL of the CPB/ZIF-8 nanocomposite can be attributed to two primary factors: (a) attachment of larger CPB NCs: as evident from the STEM images, the larger CPB NCs attached to the ZIF-8 framework contribute to the redshift in

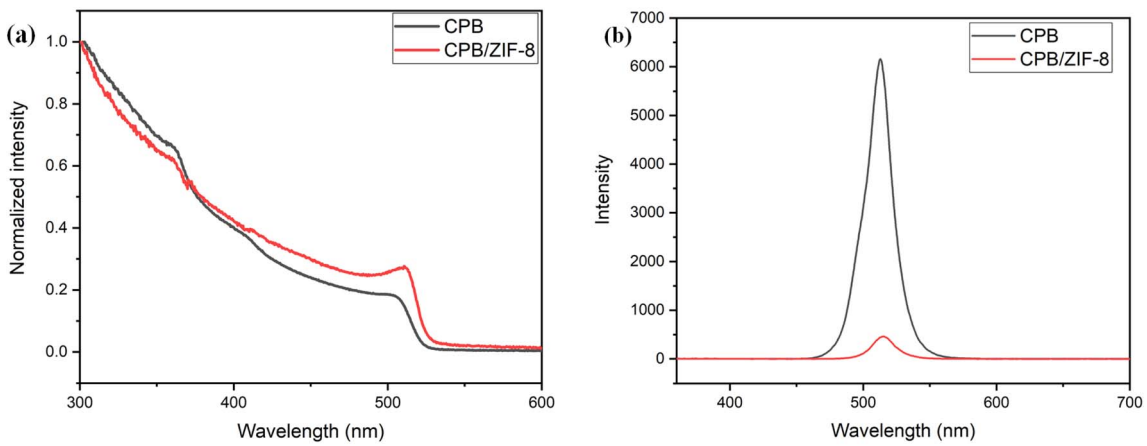

Fig. 4 (a) Absorption spectra of CPB NCs and the CPB/ZIF-8 composite, (b) PL spectra of the CPB NCs and CPB/ZIF-8 composite ($\lambda_{ex} = 320$ nm).

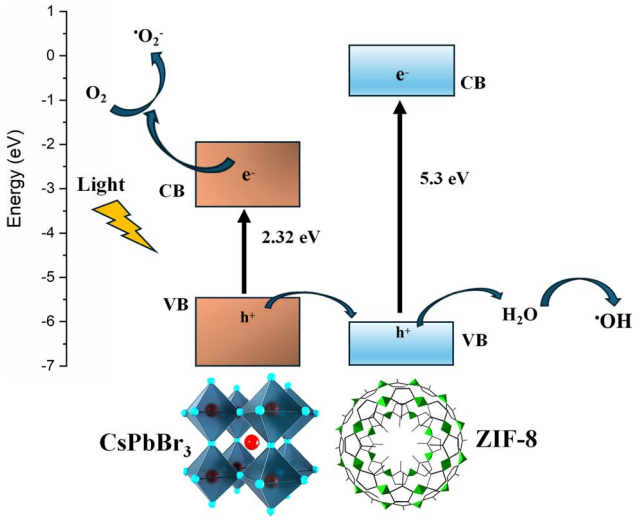

Scheme 3 The proposed charge transfer mechanism in CPB/ZIF-8 composite.

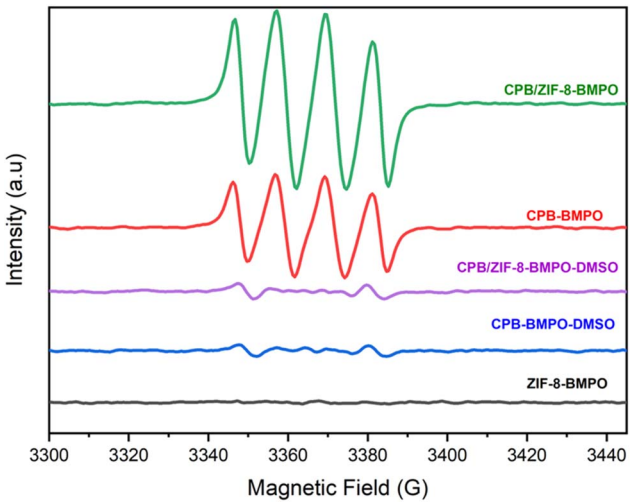

Fig. 5 EPR spectra of ZIF-8, CPB, and CPB/ZIF-8.

PL.[67] (b) Local environment changes: the interaction between the CPB NCs and the ZIF-8 framework can alter the local dielectric environment around the nanocrystals, further contributing to the shift.[68] Additionally, the CPB/ZIF-8 nanocomposite showed a significant reduction in PL intensity, quenching by 92% compared to pristine CPB NCs. This quenching effect can be attributed to charge transfer from the CPB to the ZIF-8 framework, as depicted in Scheme 3.[69–71] These results are consistent with previous reports on CPB encapsulated within ZIF-8 composites.[37,45] It was reported that the quenched PL intensity reflects inhibited radiative recombination of photogenerated carriers and effective electron transfer between CPB and ZIFs.[37] Likewise, a substantial decrease in emission intensity of CPB/ZIF-8 composites compared to pristine perovskites has been observed, indicating suppressed electron–hole recombination and enhanced charge separation in the heterojunction system.[37] This was attributed to the conduction band edge of ZIF-8 being more positive than that of CPB, which facilitates an efficient charge transfer pathway for photoelectrons.[45,72,73] Specifically, this charge transfer likely originated from the interaction between Pb^{2+} ions in CPB and nitrogen atoms in the imidazole ligands of ZIF-8.[69]

The substantial PL quenching observed in CPB/ZIF-8 composites compared to pristine CPB NCs further supports the presence of strong interactions between the nanocrystals and the framework. This robust interfacial coupling is also consistent with the FTIR results presented above and further reinforces the proposed ligand exchange mechanism. Importantly, the efficient charge separation observed in the composite may be beneficial for applications such as photocatalysis, where charge separation plays a critical role in catalytic performance.[70]

Electron paramagnetic resonance (EPR) analysis

An EPR analysis was conducted to analyze the radical formation of the CPB NCs and CPB/ZIF-8 composite. This experiment used the 5-*tert*-butoxycarbonyl-5-methyl-1-pyrroline-*n*-oxide (BMPO) as the spin trap. The EPR spectra recorded under both illuminated and dark conditions showed no radical formation for ZIF-8. On the contrary, pristine CPB NCs and the CPB/ZIF-8 composite exhibited distinct quartet paramagnetic resonance under illumination, indicating hydroxyl radical formation (Fig. 5). The absence of radical-related signals in the EPR spectra of ZIF-8 confirms its photocatalytic inactivity. In contrast, the radical generation observed in both CPB and the composite indicates that CPB is the primary contributor to the photocatalytic process.[74]

The CPB/ZIF-8 composite exhibited a stronger EPR signal than pristine CPB NCs. This enhancement suggests a higher concentration of unpaired electrons or radicals in the composite system. The increased radical formation in the composite can be attributed to improved charge transfer, as the ZIF-8 framework enhances the separation of photogenerated electrons and holes, reducing recombination and allowing more charges to participate in radical generation. This result aligns with the previously discussed PL quenching induced by the charge transfer.[75] Another factor might be the enhanced stability; the higher stability of CPB NCs within the ZIF-8 framework allows for prolonged photoactivity and sustained radical formation.[76] The EPR signals detected in both CPB and CPB/ZIF-8 composite exhibited a distinct quartet peak, indicating the presence of hydroxyl radicals ($^{\cdot}OH$).[77] Hydroxyl radicals ($^{\cdot}OH$) may form either *via* superoxide ($O_2^{\cdot -}$) reduction or directly through oxidation by photogenerated holes. To identify the dominant pathway, we employed DMSO as a selective scavenger for hole-generated $^{\cdot}OH$.[78] DMSO reacts rapidly with $^{\cdot}OH$ to form a stable methyl radical ($^{\cdot}CH_3$) but does not interact with superoxide under typical experimental conditions (Scheme S1, ESI†). The significant quenching of the EPR signal upon DMSO addition confirms that hydroxyl radicals primarily originate from photogenerated holes.[79]

The EPR measurements are carried out in the dark and under illumination (Tungsten lamp) conditions in the 10% (v/v)

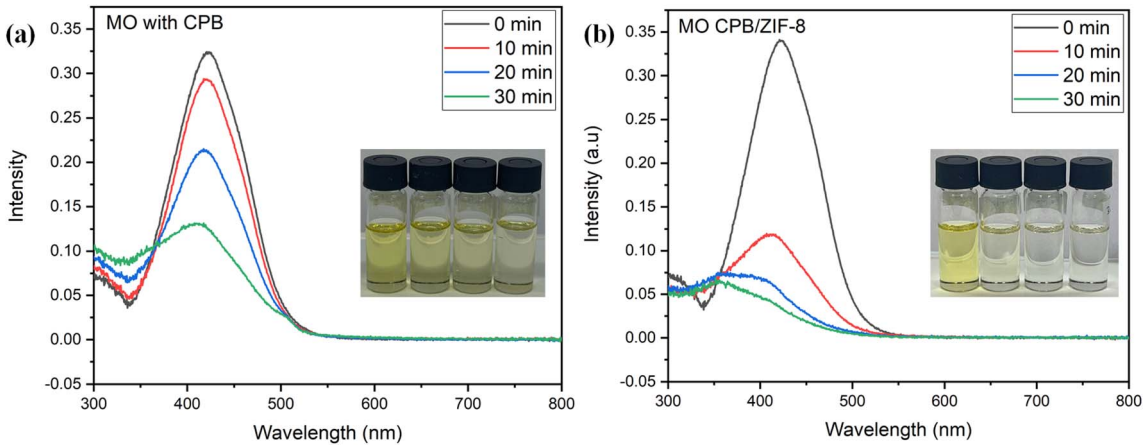

Fig. 6 The absorption spectrum shows the time-dependent degradation of MO dye with (a) CPB NCs and (b) CPB/ZIF-8 under visible light illumination.

EtOH/Toluene solution (Fig. S9†). The ZIF-8 was found to be EPR inactive, and it is due to the presence of solely Zn^{2+} ions in its crystal structure.[80] The EPR analysis reveals that the CPB/ZIF-8 composite exhibits enhanced radical formation capabilities, particularly in generating $^{\bullet}OH$. This increased radical formation efficiency can make the CPB/ZIF-8 composite a promising material for various photocatalytic applications, potentially outperforming pristine CPB NCs in effectiveness and durability.

Photocatalytic degradation studies. Following the enhanced stability supported by EPR and the PL measurement on the CPB/ZIF-8 composites, we substantiate this outcome with photocatalysis. Additionally, the strong EPR evidence of superior hydroxyl radical formation in the CPB/ZIF-8 composite reveals a promising feature for photocatalysis.

Prior to the examination of photocatalytic activity, we conducted photostability tests of CPB NCs and CPB/ZIF-8 in a 10% EtOH/toluene solution. This polar/non-polar solvent ratio was chosen to enhance the survivability of the CPB NCs. As previously reported,[81] higher ethanol content leads to rapid degradation of the nanocrystals. On the other hand, completely excluding a polar solvent would be inadequate, as it is necessary to dissolve the dye and realistically assess photocatalytic performance. The photostability was evaluated by monitoring the decrease of PL intensity over 30 minutes, with measurements taken at 10-minute intervals. The results, shown in Fig. S10–S12 in the ESI,† indicate that while the PL intensity of all samples decreased, CPB/ZIF-8 exhibited significantly less decomposition. Specifically, the PL of the pristine CPB NCs is reduced by ~39%. On the contrary, the PL of CPB/ZIF-8 showed only 5% in the dark and 18% under illumination. This data highlights the protective role of the ZIF-8 framework, suggesting improved stability for CPB/ZIF-8 compared to pristine CPB NCs. The stability of the dyes was also evaluated under dark and illumination conditions, and both dyes were stable under illumination and dark conditions without a catalyst (Fig. S13 and S14†).

We investigated the photocatalytic dye degradation capabilities of the ZIF-8, CPB NCs, and CPB/ZIF-8 composite using MO and BCG pollutants under illumination and dark conditions (Fig. 6 and S15–S19†). The selection of the dyes was based on their distinct chemical structures, which allow for a detailed evaluation of the photocatalyst's efficiency in degrading organic contaminants into non-harmful compounds. MO is an azo dye characterized by its azo (–N=N–) functional group, which is commonly found in industrial dyes and known for its persistence in the environment.[82] BCG, on the other hand, is a sulfonphthalein dye with sulfonic acid ($R–S(=O)_2–OH$) and phenol groups (C_6H_5OH), which degrade through different reaction pathways.[83]

The same solvent (10% (v/v) EtOH/toluene) conditions used for EPR analysis were also maintained for the dye degradation studies. The characteristic peaks at 421 nm for MO and 610 nm for BCG were used to monitor dye degradation. BCG also showed an additional peak at 412 nm, attributed to its monoanionic form and the pH dependency of the solution.[83,84] All dye degradation results indicated that the CPB/ZIF-8 nanocomposite exhibited superior photocatalytic activity compared to CPB NCs and ZIF-8. Specifically, CPB/ZIF-8 achieved 1.48 and 1.75 times higher degradation efficiency than CPB NCs within 30 minutes for MO and BCG dye, respectively (Fig. 7a and b). The CPB/ZIF-8 composites demonstrated a significant 1.5-times improvement in activity compared to previously reported CPB/MOF composites in the degradation of MO.[85] The degradation kinetics studies also revealed that both CPB/ZIF-8 and CPB NCs have good linear coefficients, indicating that they follow pseudo-first-order kinetics for both dyes (Fig. S20†).[86] The calculated parameters, such as the apparent rate constant, quantum efficiency (QE), and electrical energy consumption (EEC), were superior in the CPB/ZIF-8 nanocomposites. All the results regarding the photocatalysis are summarized in Table 1, with a detailed discussion included in the ESI.† The superior performance of the CPB/ZIF-8 nanocomposite can be attributed to the synergistic effect between CPB and ZIF-8, which enhances stability, increases $^{\bullet}OH$ formation, and improves overall catalytic efficiency.[75,76] This makes the CPB/ZIF-8 nanocomposite a promising material for environmental remediation applications, particularly in degrading organic dye pollutants.

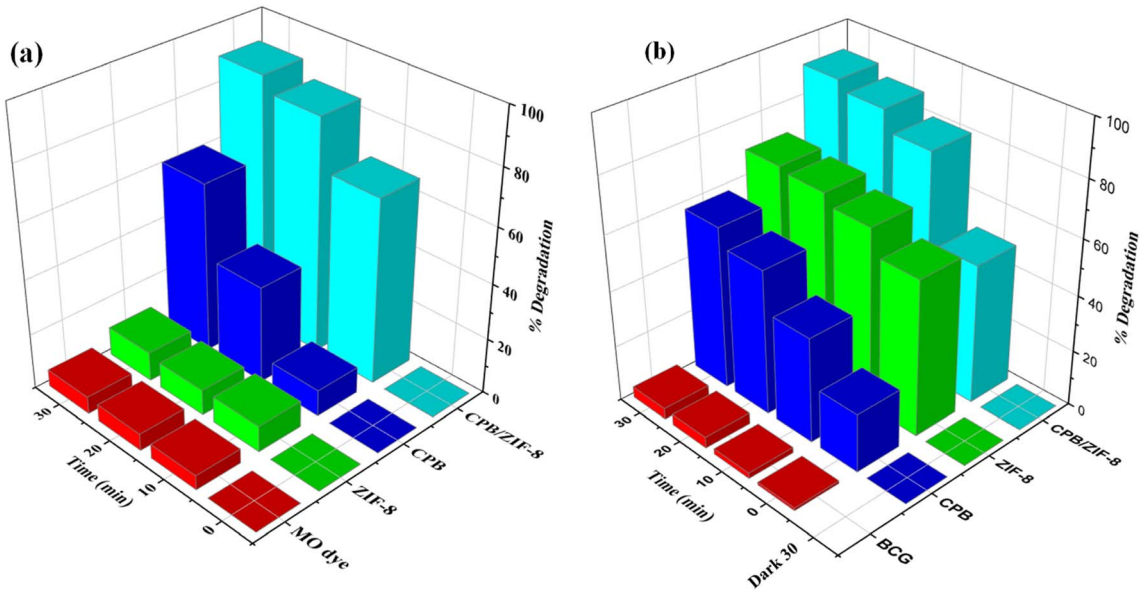

Fig. 7 Comparative degradation of (a) MO dye and (b) BCG dye with different catalysts under illumination.

Table 1 Summary of the dye degradation by using the catalysts CPB NCs and CPB/ZIF-8

Dye	Catalyst	% Degradation (30 min)	R^2	Reaction rate (min^{-1})	QE (molecules photon-1)	EEC (kW h m^{-3})
MO	CPB	61%	0.9836	0.03751 ± 0.003	0.98×10^{-3}	4.51
	CPB/ZIF-8	90.2%	0.9775	0.06485 ± 0.006	1.41×10^{-3}	1.83
BCG	CPB	47%	0.987	0.0145 ± 0.0009	0.73×10^{-3}	9.54
	CPB/ZIF-8	82.5%	0.961	0.0586 ± 0.007	1.31×10^{-3}	2.32

After conducting the dye degradation studies, the EPR results were revisited to clarify the degradation mechanism. The enhanced OH radical formation observed in the CPB/ZIF-8 nanocomposite compared to pristine CPB NCs, as confirmed by EPR, underscores the crucial role of reactive oxygen species (ROS) in the mechanism of photocatalytic degradation. This could be attributed to improved charge separation or transfer in the composite, leading to more efficient utilization of absorbed photons for ROS generation.[87,88] In contrast to pristine CPB NCs, the decrease in PL intensity observed in the composites suggests improved charge separation and charge transfer efficiency. This leads to a reduction in electron–hole recombination and an enhancement in the production of reactive species crucial for photocatalytic degradation. The formed reactive species, especially the $^{\cdot}OH$, react with dyes adsorbed on the surface of the catalysts. Previous reports regarding MO degradation also confirm the presence of OH radicals as the primary reason for its photocatalytic degradation.[89]

$$\text{CPB/ZIF-8} + h\nu \rightarrow \text{CPB/ZIF-8}\ (e^- + h^+)$$

$$O_2 + e^- \rightarrow {}^{\cdot}O_2^-$$

$$H_2O + h^+ \rightarrow {}^{\cdot}OH + H^+$$

$${}^{\cdot}O_2^- + H_2O \rightarrow {}^{\cdot}OH_2 + OH^-$$

$${}^{\cdot}OH_2 + H_2O \rightarrow H_2O_2 + {}^{\cdot}OH$$

$$H_2O_2 \rightarrow 2\ {}^{\cdot}OH\ \text{(high yield)}$$

$$\text{MO dye} + {}^{\cdot}OH/\ {}^{\cdot}O_2^- \rightarrow CO_2 + H_2O$$

Conclusion

This study highlights the successful development of a uniform distributed CPB/ZIF-8 nanocomposite, demonstrating significant improvements in photocatalytic performance. Through comprehensive analysis, we elucidated the decoration mechanism, charge transfer dynamics, and the underlying photocatalytic mechanism. The FTIR spectroscopy revealed that ligand exchange is a key mechanism in the formation of the CPB/ZIF-8 composite, where the original ligands of CPB NCs are replaced by the imidazole ligands of ZIF-8. This exchange process, driven by surface interactions, facilitates strong interfacial bonding between the CPB NCs and the ZIF-8 framework. EM analysis further corroborated the uniform distribution of CPB NCs across the ZIF-8 framework, which suggests a highly controlled attachment mechanism. This well-defined assembly is likely also driven by surface charge interactions, emphasizing the nanoscale precision of the integration process. Specifically, the NCs and ZIF-8 carry opposite partial charges, facilitating their successful attachment.

The unshifted absorption spectra, together with the TEM analysis, also confirmed that the CPB NCs remained structurally intact within the composite. Remarkably, the composite exhibited a 92% PL quenching, indicating efficient charge transfer. Moreover, EPR analysis reveals the composite's superior radical generation capabilities, particularly for $^{\bullet}OH$ formation, underscoring its potential for advanced photocatalytic applications. Notably, this study is the first to report the photocatalytic dye degradation performance of CPB/ZIF-8, demonstrating a significant enhancement under visible light irradiation, with degradation rates 1.48 and 1.75 times higher for MO and BCG, respectively, compared to pristine CPB NCs. This study provides a comprehensive understanding of the uniform decoration process, efficient charge transfer, and the enhanced photocatalytic activity of the CPB/ZIF-8 nanocomposite. Our findings establish this composite as a highly promising material for various advanced photocatalytic applications, paving the way for future research and potential real-world implementations in environmental remediation and energy conversion.

Data availability

The data supporting this article have been included as part of the ESI.†

Conflicts of interest

There are no conflicts to declare.

References

1 K. Ren, S. Yue, C. Li, Z. Fang, K. A. M. Gasem, J. Leszczynski, S. Qu, Z. Wang and M. Fan, Metal Halide Perovskites for Photocatalysis Applications, *J. Mater. Chem. A*, 2022, **10**(2), 407–429, DOI: 10.1039/d1ta09148d.

2 X. K. Liu, W. Xu, S. Bai, Y. Jin, J. Wang, R. H. Friend and F. Gao, Metal Halide Perovskites for Light-Emitting Diodes, *Nat. Mater.*, 2021, **20**(1), 10–21, DOI: 10.1038/s41563-020-0784-7.

3 Y. Fu, H. Zhu, J. Chen, M. P. Hautzinger, X. Y. Zhu and S. Jin, Metal Halide Perovskite Nanostructures for Optoelectronic Applications and the Study of Physical Properties, *Nat. Rev. Mater.*, 2019, **4**(3), 169–188, DOI: 10.1038/s41578-019-0080-9.

4 S. Schryver and A. Lamichhane, Temperature-Driven Structural Phase Transitions in $CsPbBr_3$, *Solid State Commun.*, 2023, **371**, 1–7, DOI: 10.1016/j.ssc.2023.115237.

5 S. Ullah, J. Wang, P. Yang, L. Liu, S. E. Yang, T. Xia, H. Guo and Y. Chen, All-Inorganic $CsPbBr_3$ Perovskite: A Promising Choice for Photovoltaics, *Mater. Adv.*, 2021, **2**(2), 646–683, DOI: 10.1039/d0ma00866d.

6 M. Kulbak, S. Gupta, N. Kedem, I. Levine, T. Bendikov, G. Hodes and D. Cahen, Cesium Enhances Long-Term Stability of Lead Bromide Perovskite-Based Solar Cells, *J. Phys. Chem. Lett.*, 2016, **7**(1), 167–172, DOI: 10.1021/acs.jpclett.5b02597.

7 J. Yu, G. Liu, C. Chen, Y. Li, M. Xu, T. Wang, G. Zhao and L. Zhang, Perovskite $CsPbBr_3$ Crystals: Growth and Applications, *J. Mater. Chem. C*, 2020, **8**(19), 6326–6341, DOI: 10.1039/d0tc00922a.

8 S. Arya, P. Mahajan, R. Gupta, R. Srivastava, N. K. Tailor, S. Satapathi, R. R. Sumathi, R. Datt and V. Gupta, A Comprehensive Review on Synthesis and Applications of Single Crystal Perovskite Halides, *Prog. Solid State Chem.*, 2020, **60**, 100286, DOI: 10.1016/j.progsolidstchem.2020.100286.

9 K. Liu, F. Cheng, Y. Luo, L. Liu, C. Wang, K. Xie and X. Luo, Porous Single Crystalline-like Titanium Dioxide Monolith with Enhanced Photoelectrochemical Performance, *Front. Mater.*, 2023, **10**, 1–7, DOI: 10.3389/fmats.2023.1177093.

10 J. Niu, J. Albero, P. Atienzar and H. García, Porous Single-Crystal-Based Inorganic Semiconductor Photocatalysts for Energy Production and Environmental Remediation: Preparation, Modification, and Applications, *Adv. Funct. Mater.*, 2020, **30**(15), 1–51, DOI: 10.1002/adfm.201908984.

11 S. Wang, A. A. Yousefi Amin, L. Wu, M. Cao, Q. Zhang and T. Ameri, Perovskite Nanocrystals: Synthesis, Stability, and Optoelectronic Applications, *Small Struct.*, 2021, **2**(3), 1–33, DOI: 10.1002/sstr.202000124.

12 H. Fu, Colloidal Metal Halide Perovskite Nanocrystals: A Promising Juggernaut in Photovoltaic Applications, *J. Mater. Chem. A*, 2019, **7**(24), 14357–14379, DOI: 10.1039/c8ta12509k.

13 S. Liang, M. Zhang, G. M. Biesold, W. Choi, Y. He, Z. Li, D. Shen and Z. Lin, Recent Advances in Synthesis, Properties, and Applications of Metal Halide Perovskite Nanocrystals, *Polym. Nanocompos.*, 2021, **2005888**, 1–36, DOI: 10.1002/adma.202005888.

14 A. Suhail, A. Saini, S. Beniwal and M. Bag, Tunable Optoelectronic Properties of $CsPbBr_3$ Perovskite Nanocrystals for Photodetectors Applications, *J. Phys. Chem. C*, 2023, **127**(34), 17298–17306, DOI: 10.1021/acs.jpcc.3c04856.

15 M. Giancaspro, A. Panniello, N. Depalo, R. Comparelli, M. Striccoli, M. L. Curri and E. Fanizza, Understanding the Effect of the Synthetic Method and Surface Chemistry on the Properties of $CsPbBr_3$ Nanoparticles, *Nanomaterials*, 2024, **14**(1), 1–15, DOI: 10.3390/nano14010081.

16 K. Xing, S. Cao, X. Yuan, R. Zeng, H. Li, B. Zou and J. Zhao, Thermal and Photo Stability of All Inorganic Lead Halide Perovskite Nanocrystals, *Phys. Chem. Chem. Phys.*, 2021, **23**(32), 17113–17128, DOI: 10.1039/d1cp02119b.

17 C. Otero-Martínez, N. Fiuza-Maneiro and L. Polavarapu, Enhancing the Intrinsic and Extrinsic Stability of Halide Perovskite Nanocrystals for Efficient and Durable Optoelectronics, *ACS Appl. Mater. Interfaces*, 2022, **14**(30), 34291–34302, DOI: 10.1021/acsami.2c01822.

18 C. G. Sanjayan, M. S. Jyothi and R. G. Balakrishna, Stabilization of $CsPbBr_3$ Quantum Dots for Photocatalysis, Imaging and Optical Sensing in Water and Biological Medium: A Review, *J. Mater. Chem. C*, 2022, **10**, 6935–6956, DOI: 10.1039/d2tc00340f.

19 N. Prasad, A. Leybovich, A. Goldreich, H. Shalom, J. Prilusky, A. Puravankara, A. Sam Thomas, D. Bograchev and L. Yadgarov, Optimized Growth and Manipulation of Light-

Matter Interaction in Stabilized Halide Perovskite Nanowire Array, *Adv. Opt. Mater.*, 2025, 2402976, DOI: 10.1002/adom.202402976.

20 C. Zhang, W. Li and L. Li, Metal Halide Perovskite Nanocrystals in Metal-Organic Framework Host: Not Merely Enhanced Stability, *Angew. Chem.*, 2021, **133**(14), 7564–7577, DOI: 10.1002/ange.202006169.

21 K. S. Park, Z. Ni, A. P. Côté, J. Y. Choi, R. Huang, F. J. Uribe-Romo, H. K. Chae, M. O'Keeffe and O. M. Yaghi, Exceptional Chemical and Thermal Stability of Zeolitic Imidazolate Frameworks, *Proc. Natl. Acad. Sci. U. S. A.*, 2006, **103**(27), 10186–10191, DOI: 10.1073/pnas.0602439103.

22 Y. R. Lee, M. S. Jang, H. Y. Cho, H. J. Kwon, S. Kim and W. S. Ahn, ZIF-8: A Comparison of Synthesis Methods, *Chem. Eng. J.*, 2015, **271**, 276–280, DOI: 10.1016/j.cej.2015.02.094.

23 J. Hou, Z. Wang, P. Chen, V. Chen, A. K. Cheetham and L. Wang, Intermarriage of Halide Perovskites and Metal-Organic Framework Crystals, *Angew. Chem., Int. Ed.*, 2020, **59**(44), 19434–19449, DOI: 10.1002/anie.202006956.

24 C. C. Chueh, C. I. Chen, Y. A. Su, H. Konnerth, Y. J. Gu, C. W. Kung and K. C. W. Wu, Harnessing MOF Materials in Photovoltaic Devices: Recent Advances, Challenges, and Perspectives, *J. Mater. Chem. A*, 2019, **7**(29), 17079–17095, DOI: 10.1039/c9ta03595h.

25 Z. D. Lian, B. Wang, Z. S. Wu, H. Lin, S. S. Yan, J. L. Li, K. Zhang, Q. G. Zeng, J. C. Xu, S. Chen, S. P. Wang and K. W. Ng, Highly Stable $CsPbBr_3$ Perovskite Nanocrystals Encapsulated in Metal-Organic Frameworks for White Light-Emitting Diodes, *ACS Appl. Nano Mater.*, 2023, **6**(3), 1808–1816, DOI: 10.1021/acsanm.2c04758.

26 J. N. Huang, Y. J. Dong, H. B. Zhao, H. Y. Chen, D. B. Kuang and C. Y. Su, Efficient Encapsulation of $CsPbBr_3$ and Au Nanocrystals in Mesoporous Metal-Organic Frameworks towards Synergetic Photocatalytic CO_2 Reduction, *J. Mater. Chem. A*, 2022, **10**(47), 25212–25219, DOI: 10.1039/d2ta06561d.

27 W. Lv, L. Li, M. Xu, J. Hong, X. Tang, L. Xu, Y. Wu, R. Zhu, R. Chen and W. Huang, Improving the Stability of Metal Halide Perovskite Quantum Dots by Encapsulation, *Adv. Mater.*, 2019, **31**(28), 1–28, DOI: 10.1002/adma.201900682.

28 J. Zhang, W. Zhou, J. Chen and Y. Li, Encapsulating Halide Perovskite Quantum Dots in Metal-Organic Frameworks for Efficient Photocatalytic CO_2 Reduction, *Catalysts*, 2024, **14**(9), 1–15, DOI: 10.3390/catal14090590.

29 J. K George, K. Gayathri, A. Pasha, S. Mohan and R. G. Balakrishna, Binding of $CsPbBr_3$ Nanocrystals to MOF-5 for the Detection of Cadmium Ions in Aqueous Media, *ACS Appl. Nano Mater.*, 2023, **6**(11), 9464–9474, DOI: 10.1021/acsanm.3c01158.

30 L. Hong, J. Cao, W. Zhang, T. Jiang, G. Pan and Y. Wu, The Development and Synthesis of a CdZnS @Metal–Organic Framework ZIF-8 for the Highly Efficient Photocatalytic Degradation of Organic Dyes, *Molecules*, 2023, **28**(23), 1–12, DOI: 10.3390/molecules28237904.

31 Y. Zheng, T. Gao, S. Chen, C. T. J. Ferguson, K. A. I. Zhang, F. Fang, Y. Shen, N. A. Khan, L. Wang and L. Ye, $CsPbBr_3$ Quantum Dots-Decorated Porous Covalent Triazine Frameworks Nanocomposites for Enhanced Solar-Driven H_2O_2 Production, *Compos. Commun.*, 2022, **36**, 1–6, DOI: 10.1016/j.coco.2022.101390.

32 S. Wan, M. Ou, Q. Zhong and X. Wang, Perovskite-Type $CsPbBr_3$ Quantum Dots/UiO-66(NH_2) Nanojunction as Efficient Visible-Light-Driven Photocatalyst for CO_2 Reduction, *Chem. Eng. J.*, 2019, **358**, 1287–1295, DOI: 10.1016/j.cej.2018.10.120.

33 R. Cheng, E. Debroye, J. Hofkens and M. B. J. Roeffaers, Efficient Photocatalytic CO_2 Reduction with MIL-100(Fe)-$CsPbBr_3$ Composites, *Catalysts*, 2020, **100**(10), 1–13.

34 J. Leng, T. Wang, Z. K. Tan, Y. J. Lee, C. C. Chang and K. Tamada, Tuning the Emission Wavelength of Lead Halide Perovskite NCs *via* Size and Shape Control, *ACS Omega*, 2022, **7**(1), 565–577, DOI: 10.1021/acsomega.1c05001.

35 S. Ahmed, D. Mohanta, K. Baruah and S. K. Dolui, $CsPbBr_3$ Perovskite Quantum Dot Decorated ZIF-8 MOF: A Selective Dual Recognition Fluorometric Visual Probe for 4-Nitroaniline and Rhodamine Blue, *Anal. Methods*, 2023, **15**(46), 6394–6403, DOI: 10.1039/d3ay01458d.

36 A. Akhundzadeh Tezerjani, R. Halladj and S. Askari, Different View of Solvent Effect on the Synthesis Methods of Zeolitic Imidazolate Framework-8 to Tuning the Crystal Structure and Properties, *RSC Adv.*, 2021, **11**(32), 19914–19923, DOI: 10.1039/d1ra02856a.

37 S. N. Guo, D. Wang and J. X. Wang, ZIF-8@$CsPbBr_3$ Nanocrystals Formed by Conversion of Pb to $CsPbBr_3$ in Bimetallic MOFs for Enhanced Photocatalytic CO_2 Reduction, *Small Methods*, 2024, **8**(10), 1–8, DOI: 10.1002/smtd.202301508.

38 Y. Lu, R. Xiong, X. Lin, L. Zhang, X. Meng and Z. Luo, $CsPbBr_3$ NCs Confined and *In Situ* Grown in ZIF-8: A Stable, Sensitive, Reliable Fluorescent Sensor for Evaluating the Acid Value of Edible Oils, *ACS Appl. Mater. Interfaces*, 2024, **16**(32), 42772–42782, DOI: 10.1021/acsami.4c10280.

39 L. Zhao, G. Niu, F. Gao, K. Lu, Z. Sun, H. Li, M. Stenzel, C. Liu and Y. Jiang, Gold Nanorods (AuNRs) and Zeolitic Imidazolate Framework-8 (ZIF-8) Core-Shell Nanostructure-Based Electrochemical Sensor for Detecting Neurotransmitters, *ACS Omega*, 2021, **6**(48), 33149–33158, DOI: 10.1021/acsomega.1c05529.

40 S. Hui, Q. Liu, Z. Huang, J. Yang, Y. Liu and S. Jiang, Gold Nanoclusters-Decorated Zeolitic Imidazolate Frameworks with Reactive Oxygen Species Generation for Photoenhanced Antibacterial Study, *Bioconjugate Chem.*, 2020, **31**(10), 2439–2445, DOI: 10.1021/acs.bioconjchem.0c00485.

41 K. Rokesh, M. Sakar and T. O. Do, Emerging Hybrid Nanocomposite Photocatalysts for the Degradation of Antibiotics: Insights into Their Designs and Mechanisms, *Nanomaterials*, 2021, **11**(3), 1–34, DOI: 10.3390/nano11030572.

42 H. Li, Y. Ding, K. Luo, Q. Zhang, H. Yuan, S. Xu and M. Xu, Controllable Surface Carrier Type of Metal Oxide

Nanocrystals for Multifunctional Photocatalysis, *iScience*, 2025, **28**(2), 111750, DOI: 10.1016/j.isci.2025.111750.

43 A. Goldreich, J. Prilusky, N. Prasad and L. Yadgarov, Highly Stable $CsPbBr_3$@MoS_2 Nanostructures: Synthesis and Optoelectronic Properties Towards Implementation into Solar Cells, *Small*, 2024, **20**(40), 1–11, DOI: 10.1002/smll.202404727.

44 M. Imran, P. Ijaz, L. Goldoni, D. Maggioni, U. Petralanda, M. Prato, G. Almeida, I. Infante and L. Manna, Simultaneous Cationic and Anionic Ligand Exchange for Colloidally Stable $CsPbBr_3$ Nanocrystals, *ACS Energy Lett.*, 2019, **4**(4), 819–824, DOI: 10.1021/acsenergylett.9b00140.

45 Z. C. Kong, J. F. Liao, Y. J. Dong, Y. F. Xu, H. Y. Chen, D. B. Kuang and C. Y. Su, Core@shell $CsPbBr_3$@zeolitic Imidazolate Framework Nanocomposite for Efficient Photocatalytic CO_2 Reduction, *ACS Energy Lett.*, 2018, **3**(11), 2656–2662, DOI: 10.1021/acsenergylett.8b01658.

46 K. Vighnesh, S. Wang, H. Liu and A. L. Rogach, Hot-Injection Synthesis Protocol for Green-Emitting Cesium Lead Bromide Perovskite Nanocrystals, *ACS Nano*, 2022, **16**(12), 19618–19625, DOI: 10.1021/acsnano.2c11689.

47 N. A. Murugan, S. Schrader and H. Ågren, Role of Protonation State and Solvation on the Ph Dependent Optical Properties of Bromocresol Green, *J. Chem. Theory Comput.*, 2014, **10**(9), 3958–3968, DOI: 10.1021/ct500375x.

48 J. Pradhan, P. Moitra, Umesh, B. Das, P. Mondal, G. S. Kumar, U. K. Ghorai, S. Acharya and S. Bhattacharya, Encapsulation of $CsPbBr_3$ Nanocrystals by a Tripodal Amine Markedly Improves Photoluminescence and Stability Concomitantly *via* Anion Defect Elimination, *Chem. Mater.*, 2020, **32**(17), 7159–7171, DOI: 10.1021/acs.chemmater.0c00385.

49 Q. Zhong, M. Cao, Y. Xu, P. Li, Y. Zhang, H. Hu, D. Yang, Y. Xu, L. Wang, Y. Li, X. Zhang and Q. Zhang, L-Type Ligand-Assisted Acid-Free Synthesis of $CsPbBr_3$ Nanocrystals with Near-Unity Photoluminescence Quantum Yield and High Stability, *Nano Lett.*, 2019, **19**(6), 4151–4157, DOI: 10.1021/acs.nanolett.9b01666.

50 V. Viswanathan, T. Laha, K. Balani, A. Agarwal and S. Seal, Challenges and Advances in Nanocomposite Processing Techniques, *Mater. Sci. Eng., R*, 2006, **54**(5–6), 121–285, DOI: 10.1016/j.mser.2006.11.002.

51 Y. Wang, G. J. Desroches and R. J. Macfarlane, Ordered Polymer Composite Materials: Challenges and Opportunities, *Nanoscale*, 2021, **13**(2), 426–443, DOI: 10.1039/d0nr07547g.

52 I. W. M. Smith, The Temperature-Dependence of Elementary Reaction Rates: Beyond Arrhenius, *Chem. Soc. Rev.*, 2008, **37**(4), 812–826, DOI: 10.1039/b704257b.

53 J. B. Ferguson, G. Kaptay, B. F. Schultz, P. K. Rohatgi, K. Cho and C. S. Kim, Brownian Motion Effects on Particle Pushing and Engulfment during Solidification in Metal-Matrix Composites, *Metall. Mater. Trans. A*, 2014, **45**(10), 4635–4645, DOI: 10.1007/s11661-014-2379-x.

54 H. Wu, Y. Zhang, M. Lu, X. Zhang, C. Sun, T. Zhang, V. L. Colvin and W. W. Yu, Surface Ligand Modification of Cesium Lead Bromide Nanocrystals for Improved Light-Emitting Performance, *Nanoscale*, 2018, **10**(9), 4173–4178, DOI: 10.1039/c7nr09126e.

55 S. Toso, D. Baranov and L. Manna, Metamorphoses of Cesium Lead Halide Nanocrystals, *Acc. Chem. Res.*, 2021, **54**(3), 498–508, DOI: 10.1021/acs.accounts.0c00710.

56 A. Kipkorir, J. Dubose, J. Cho and P. V. Kamat, $CsPbBr_3$-CdS Heterostructure: Stabilizing Perovskite Nanocrystals for Photocatalysis, *Chem. Sci.*, 2021, **12**(44), 14815–14825, DOI: 10.1039/d1sc04305f.

57 N. K. Maddigan, A. Tarzia, D. M. Huang, C. J. Sumby, S. G. Bell, P. Falcaro and C. J. Doonan, Protein Surface Functionalisation as a General Strategy for Facilitating Biomimetic Mineralisation of ZIF-8, *Chem. Sci.*, 2018, **9**(18), 4217–4223, DOI: 10.1039/c8sc00825f.

58 J. De Roo, M. Ibáñez, P. Geiregat, G. Nedelcu, W. Walravens, J. Maes, J. C. Martins, I. Van Driessche, M. V. Kovalenko and Z. Hens, Highly Dynamic Ligand Binding and Light Absorption Coefficient of Cesium Lead Bromide Perovskite Nanocrystals, *ACS Nano*, 2016, **10**(2), 2071–2081, DOI: 10.1021/acsnano.5b06295.

59 S. Mei, B. Yang, X. Wei, H. Dai, Z. Chen, Z. Cui, G. Zhang, F. Xie, W. Zhang and R. Guo, Facile Synthesis and Optical Properties of $CsPbX_3$/ZIF-8 Composites for Wide-Color-Gamut Display, *Nanomaterials*, 2019, **9**(6), 1–10, DOI: 10.3390/nano9060832.

60 A. Paul, G. Vyas, P. Paul and D. N. Srivastava, Gold-Nanoparticle-Encapsulated Zif-8 for a Mediator-Free Enzymatic Glucose Sensor by Amperometry, *ACS Appl. Nano Mater.*, 2018, **1**(7), 3600–3607, DOI: 10.1021/acsanm.8b00748.

61 B. Hudait, S. K. Dutta and N. Pradhan, Isotropic $CsPbBr_3$ Perovskite Nanocrystals beyond Nanocubes: Growth and Optical Properties, *ACS Energy Lett.*, 2020, **5**(2), 650–656, DOI: 10.1021/acsenergylett.9b02729.

62 S. Toso, D. Baranov, C. Giannini, S. Marras and L. Manna, Wide-Angle X-Ray Diffraction Evidence of Structural Coherence in $CsPbBr_3$ Nanocrystal Superlattices, *ACS Mater. Lett.*, 2019, **1**(2), 272–276, DOI: 10.1021/acsmaterialslett.9b00217.

63 A. Schejn, A. Aboulaich, L. Balan, V. Falk, J. Lalevée, G. Medjahdi, L. Aranda, K. Mozet and R. Schneider, Cu^{2+}-Doped Zeolitic Imidazolate Frameworks (ZIF-8): Efficient and Stable Catalysts for Cycloadditions and Condensation Reactions, *Catal. Sci. Technol.*, 2015, **5**, 1829–1839, DOI: 10.1039/c4cy01505c.

64 X. Wang, W. Liu, J. He, Y. Li and Y. Liu, Synthesis of All-Inorganic Halide Perovskite Nanocrystals for Potential Photoelectric Catalysis Applications, *Catalysts*, 2023, **13**(7), 1–13, DOI: 10.3390/catal13071041.

65 H. Chen, R. Li, A. Guo and Y. Xia, Highly Fluorescent $CsPbBr_3/TiO_2$ Core/Shell Perovskite Nanocrystals with Excellent Stability, *SN Appl. Sci.*, 2021, **3**(6), 1–7, DOI: 10.1007/s42452-021-04648-8.

66 S. K. Sharma, D. S. Verma, L. U. Khan, S. Kumar and S. B. Khan, Fourier Transform Infrared Spectroscopy: Fundamentals and Application in Functional Groups and Nanomaterials Characterization, in *Handbook of Materials*

Characterization, 2018, pp. 1–613, DOI: 10.1007/978-3-319-92955-2.

67 M. C. Brennan, J. E. Herr, T. S. Nguyen-Beck, J. Zinna, S. Draguta, S. Rouvimov, J. Parkhill and M. Kuno, Origin of the Size-Dependent Stokes Shift in $CsPbBr_3$ Perovskite Nanocrystals, *J. Am. Chem. Soc.*, 2017, **139**(35), 12201–12208, DOI: 10.1021/jacs.7b05683.

68 H. Liu and S. Bansal, Metal Halide Perovskite Nanostructures and Quantum Dots for Photocatalytic CO_2 Reduction: Prospects and Challenges, *Mater. Today Energy*, 2023, **32**, 101230, DOI: 10.1016/j.mtener.2022.101230.

69 M. Xin, Y. Fu, Y. Zhou, J. Han, Y. Mao, M. Li, J. Liu and M. Huang, The Surface-Enhanced Raman Scattering of All-Inorganic Perovskite Quantum Dots of $CsPbBr_3$, *New J. Chem.*, 2020, **44**, 17570–17576, DOI: 10.1039/d0nj03587d.

70 S. Ray, M. R. Sahoo, S. Mukherjee, A. Perumal, S. K. Nayak and S. Bhaumik, Understanding the Charge Transfer Mechanism in $CsPbBr_3$ Nanocrystals and Nitrogen-Doped Carbon Quantum Dot Heterostructures: Effect of Nanocrystal Encapsulation, *RSC Adv.*, 2023, **13**(50), 35551–35561, DOI: 10.1039/d3ra06307k.

71 Y. Wang, G. Xu, X. Zhang, X. Yang, H. Hou, W. Ai and L. Zhao, N- and S-Codoped Carbon Quantum Dots for Enhancing Fluorescence Sensing of Trace Hg2+, *Phys. Chem. Chem. Phys.*, 2023, **25**(41), 28230–28240, DOI: 10.1039/d3cp02924g.

72 S. Bourne-Worster, Charge Transfer as a Mechanism for Chlorophyll Fluorescence Concentration Quenching, *Proc. Natl. Acad. Sci. U. S. A.*, 2023, **120**(5), 1–9, DOI: 10.1073/pnas.2210811120.

73 S. Ray, M. R. Sahoo, S. Mukherjee, A. Perumal, S. K. Nayak and S. Bhaumik, Understanding the Charge Transfer Mechanism in Nanocrystal Encapsulation †, *RSC Adv.*, 2023, 35551–35561, DOI: 10.1039/d3ra06307k.

74 A. Sedova, P. N. Immanuel, R. Carmieli, H. Shalom, A. S. Thomas, J. Prilusky, A. Puravankara and I. Bar-on, Exploring Halide Perovskite Nanocrystal Decomposition : Insight by In-Situ Electron Paramagnetic Resonance Spectroscopy, *ChemRxiv*, 2024, 1–29.

75 X. Li, L. Yang, X. Wang, J. Zhang, L. Xie, L. Deng, G. Zhang and J. Jiang, Charge Steering in Heterojunction Photocatalysis : General Principles, Design, Construction, and Challenges, *Small Sci.*, 2023, **2200041**(3), 1–24, DOI: 10.1002/smsc.202200041.

76 H. Li, C. Lai, Z. Wei, X. Zhou, S. Liu, L. Qin, H. Yi, Y. Fu, L. Li, M. Zhang, F. Xu, H. Yan, M. Xu, D. Ma and Y. Li, Chemosphere Strategies for Improving the Stability of Perovskite for Photocatalysis : A Review of Recent Progress, *Chemosphere*, 2023, **344**, 140395, DOI: 10.1016/j.chemosphere.2023.140395.

77 S. E. Lehman, A. S. Morris, P. S. Mueller, A. K. Salem, V. H. Grassian and S. C. Larsen, Silica Nanoparticle-Generated ROS as a Predictor of Cellular Toxicity: Mechanistic Insights and Safety by Design, *Environ. Sci.:Nano*, 2016, **3**(1), 56–66, DOI: 10.1039/c5en00179j.

78 M. K. Eberhardt and R. Colina, The Reaction of OH Radicals with Dimethyl Sulfoxide. A Comparative Study of Fenton's Reagent and the Radiolysis of Aqueous Dimethyl Sulfoxide Solutions, *J. Org. Chem.*, 1988, (7), 1071–1074.

79 M. G. Steiner and C. F. Babbs, Quantitation of the Hydroxyl Radical by Reaction with Dimethyl Sulfoxide, *Arch. Biochem. Biophys.*, 1990, **278**(2), 478–481, DOI: 10.1016/0003-9861(90)90288-A.

80 N. Nagarjun and A. Dhakshinamoorthy, A Cu-Doped ZIF-8 Metal-Organic Framework as a Heterogeneous Solid Catalyst for Aerobic Oxidation of Benzylic Hydrocarbons, *New J. Chem.*, 2019, **43**(47), 18702–18712, DOI: 10.1039/c9nj03698a.

81 A. Sedova, P. N. Immanuel, R. Carmieli, H. Shalom, A. Goldreich, A. S. Thomas, J. Prilusky, A. Puravankara, I. Bar-on and L. Yadgarov, Exploring Halide Perovskite Nanocrystal Decomposition : Insight by in- Situ Electron Paramagnetic Resonance Spectroscopy, *Nano Res.*, 2025, **94907210**, 1–11, DOI: 10.26599/NR.2025.94907210.

82 R. H. Waghchaure, V. A. Adole and B. S. Jagdale, Photocatalytic Degradation of Methylene Blue, Rhodamine B, Methyl Orange and Eriochrome Black T Dyes by Modified ZnO Nanocatalysts: A Concise Review, *Inorg. Chem. Commun.*, 2022, **143**, 109764, DOI: 10.1016/j.inoche.2022.109764.

83 P. N. Immanuel, S. Huang, P. Taank, A. Goldreich, J. Prilusky, A. Byregowda, R. Carmieli, H. Shalom, A. Leybovich, A. Zak, N. Aggarwal, K. V. Adarsh and L. Yadgarov, Enhanced Photocatalytic Activity of Cs_4PbBr_6/WS_2 Hybrid Nanocomposite, *Adv. Energy Sustainability Res.*, 2024, **5**(2), 1–11, DOI: 10.1002/aesr.202300193.

84 H. Lee, Y. K. Park, S. J. Kim, B. H. Kim, H. S. Yoon and S. C. Jung, Rapid Degradation of Methyl Orange Using Hybrid Advanced Oxidation Process and Its Synergistic Effect, *J. Ind. Eng. Chem.*, 2016, **35**, 205–210, DOI: 10.1016/j.jiec.2015.12.037.

85 C. Zhang, J. Miao, L. Guo, T. Tan, W. Cai, X. Lei, Y. Li and Z. Wang, Based on Z-Scheme Heterojunction CsPbBr3/UiO-66 Composite Photocatalytic Degradation, *Appl. Organomet. Chem.*, 2023, **37**(7), 1–12, DOI: 10.1002/aoc.7122.

86 A. S. Yusuff, L. T. Popoola and E. I. Aderibigbe, Solar Photocatalytic Degradation of Organic Pollutants in Textile Industry Wastewater by ZnO/Pumice Composite Photocatalyst, *J. Environ. Chem. Eng.*, 2020, **8**(4), 1–8, DOI: 10.1016/j.jece.2020.103907.

87 R. Marschall, Semiconductor Composites: Strategies for Enhancing Charge Carrier Separation to Improve Photocatalytic Activity, *Adv. Funct. Mater.*, 2014, **24**(17), 2421–2440, DOI: 10.1002/adfm.201303214.

88 H. Park, H. I. Kim, G. H. Moon and W. Choi, Photoinduced Charge Transfer Processes in Solar Photocatalysis Based on Modified TiO_2, *Energy Environ. Sci.*, 2016, **9**(2), 411–433, DOI: 10.1039/c5ee02575c.

89 W. Li, D. Li, Y. Lin, P. Wang, W. Chen, X. Fu and Y. Shao, Evidence for the Active Species Involved in the Photodegradation Process of Methyl Orange on TiO_2, *J. Phys. Chem. C*, 2012, **116**(5), 3552–3560, DOI: 10.1021/jp209661d.